Bio-inspired Surface Texture Fluid Drag Reduction using Large Eddy Simulation

S. Hijazi and E. Tolouei[†]

School of Engineering, Emirates Aviation University, Dubai, United Arab Emirates

†*Corresponding Author Email: elham.tolouei@eau.ac.ae*

ABSTRACT

Skin friction drag can be reduced through the application of bio-inspired riblet surfaces. Numerical simulations were performed using Large Eddy Simulation (LES) to investigate the effect of using riblets on reducing skin friction drag. In this study, three different riblet configurations were used; scalloped, sawtooth and a new design, hybrid, riblet. To validate the effect of using the proposed hybrid riblet design compared with other riblets used in the literature; before applying to complex geometries, they were initially applied to a flat plate in parallel arrangement. Results showed skin friction coefficient reduction of 14% using the proposed hybrid riblet. This reduction was 9.2 times and 1.2 times more compared to sawtooth and scalloped configurations, respectively. The hybrid riblet was then applied partially and fully to NACA 0012 airfoil. Skin friction coefficient reduction of 34.5% was obtained when the hybrid riblet fully applied on the airfoil surface. Furthermore, the Convergent-Divergent (C-D) arrangement was studied, where the riblets were placed fully on the NACA 0012 and aligned with a yaw angle with respect to the flow direction. The convergent lines are inspired by the sensory part of the shark skin, whereas the divergent lines or herringbone are found on the bird feather. The two different riblet configurations, sawtooth and hybrid were modeled with the C-D arrangement and the hybrid riblet with C-D arrangement contributed to higher skin friction coefficient reduction, 34.5%, than the sawtooth riblet shape, 26.75%. Moreover, the C-D arrangement was compared to the parallel arrangement and shown that the C-D arrangement increased the lift coefficient (C_l) of the airfoil, the flow separation was delayed and the overall performance of the airfoil was enhanced.

Keywords: Computational fluid dynamics; Large eddy simulation; Riblets; Drag reduction; Aerodynamic efficiency NACA0012.

NOMENCLATURE

CFD	Computational Fluid Dynamic	s^+	non-dimensional spacing of a riblet
C_d	drag coefficient	SST	Shear Stress Transport
C_f	skin friction coefficient	t	thickness of a riblet
C_l	lift coefficient	t^+	non-dimensional thickness of a riblet
C_m	moment coefficient	U_∞	freestream velocity
C-D	Convergent-Divergent	V_τ	shear stress velocity
h	height of a riblet	WALE	Wall-Adapting Local Eddy-viscosity
h^+	non-dimensional height of a riblet	α	angle of attack
I	turbulence intensity	γ	yaw angle
l	turbulence length-scale	δ	boundary layer thickness
LES	Large Eddy Simulation	ν	kinematic viscosity
RANS	Reynolds-Averaged Navier-Stokes	ρ	fluid density
Re	Reynolds Number	τ_0	wall shear stress
s	spacing of a riblet		

1. INTRODUCTION

Nature is full of examples of structures, materials and surfaces whose feature can be exploited for commercial application. Biomimetics or mimic biology, is the study of naturally occurring properties of plants and animals for the purpose of inspired designs. Properties of biological materials and surface structures are resulted from a complicated networking between surface architecture and

physical and chemical properties (Bhushan 2009, 2016). Surface microstructures play an important role in modern technology specifically in aviation and marine industries to reduce drag force and fuel consumption (Caram and Ahmed 1991; Jimenez 1994; Sundaram et al. 1996; Bechert and Hage 2006; Bhushan 2009; Fu et al. 2017; Ibrahim et al. 2018; Catalano et al. 2020) and in wind engineering field (Leitl et al. 2020a,b). Geometry of these microstructures is inspired by nature, *i.e.* fast-swimming shark skin, which is covered with tiny scales known as dermal denticles shaped like small riblets. These riblets, which are aligned with the fluid flow direction have been studied by many researchers.

Studies conducted by Walsh (1983), Caram and Ahmed (1991), Bechert et al. (1997), Dean and Bhushan (2010), Bixler and Bhushan (2013), Martin and Bhushan (2016b) and Husen et al. (2020) on a flat plate and various airfoil shapes at different Reynolds numbers have shown a drag reduction benefit up to 10% using shark-skin inspired riblets. They have shown the drag reduction depends on the non-dimensionalised height (h^+) and spacing (s^+) of the riblet geometry.

Walsh (1983) has proved that an optimal drag reduction of 8% occurs for a flat plate when h^+=8-10 and s^+=15-20. Caram and Ahmed (1991) have shown a 13.3% maximum net drag reduction on NACA 0012 airfoil by using riblets of h^+=8, mainly due to the reduction of skin friction drag. Walsh (1983) and Caram and Ahmed (1991) have used a sawtooth riblet geometry for their study. Bechert et al. (1997) and Dean and Bhushan (2010) have studied the effect of different riblet geometries, *i.e.* sawtooth, scalloped, and blade riblets on drag reduction. They showed that the blade riblet configuration has the highest drag reduction compare to the other riblet geometries. Bixler and Bhushan (2013) research using experimental technique on continues and segmented blade riblets showed similar drag reduction results. Martin and Bhushan (2016a) have also shown that blade geometry had the highest drag reduction of 11.6% followed by scalloped at 5.7% and sawtooth at 4.1%. All their models had constant height of h^+=8 and varying spacing of s^+=8.3-41.1. They have revealed that optimized riblet configurations for commercial applications should be with spacing s^+=15-20 and height of h^+=8-10 to achieve the greatest drag reduction in order of 10%.

Sundaram et al. (1996) have reported higher skin friction reduction of 16% for NACA 0012 compares to a flat plate while the flow becomes turbulent. Their results have implied increased effectiveness of riblets in adverse pressure gradient regions. The riblet film was then applied to a swept wing (Sundaram et al. 1999) and realized the importance of aligning the riblets along the local surface streamline direction on a swept wing (for example, corresponding to cruise conditions) to fully utilize the benefits of riblet action.

An alternative investigation to simplified standard riblet geometry is riblets arranged with a yaw angle,

γ, to express the angle between the flow direction and aligned riblets, which is called C-D arrangement (Xu et al. 2018, Benschop and Breugem 2017, Park and Choi 2017, and Koeltzsch et al. 2002). C-D riblet arrangement is the new design pattern, which begins to attract researchers recently. In this type of riblet arrangement, section of the riblet with a negative yaw angle and a positive yaw angle with respect to the freestream direction are arranged in an alternative manner in the spanwise direction. Convergent riblet pattern is found upstream of the sensory receptors of sharks, whereas the diverging riblet pattern or herringbone is observed upstream of the hearing sensors of these animals (Koeltzsch et al. 2002). It also appears on the secondary flight feathers of different species of birds (Chen et al. 2014, 2013).

Not only external flow, but also internal flow has been studied to investigate the effect of riblets on drag reduction. Koeltzsch et al. (2002) have studied the flow in a circular pipe, which one half of the inner wall of the pipe was covered with riblets film aligned with a $-45°$ yaw angle and $+45°$ yaw angle in the other half. An increase in the local streamwise velocity and decrease in turbulent fluctuations over the diverging riblet pattern plus 17% reduction in turbulent skin friction drag were observed. Experimental investigation has carried out by Chen et al. (2014) in a fully developed turbulent pipe flow covered with C-D arrangement, yaw angle of $30°$. Their results show 21% drag reduction, which is significantly larger than the drag reduction obtained using longitudinal riblet arrangement in the work of Walsh (1983) and Bechert et al. (1997).

Reduction in pressure loss using herringbone riblets has been shown by Liu et al. (2017). They have observed that fixing the riblets on the suction surface of highly loaded diffuser blades can lead to reduce pressure loss and increase the flow turning angle in a linear cascade. Vortices generated by these riblets play an important role in suppressing the flow separation occurring on the suction surface.

All previous research proved that drag reduction capability of riblets is effective in turbulent flow, therefore proper numerical strategy and turbulent model in numerical simulation are crucial. Previously, different turbulent models have been applied to study the riblet effect, such as modified Spalart-Allmaras model (Aupoix et al. 2012; Koepplin et al. 2017), $k-\varepsilon$ turbulent model (Mele and Tognaccini 2012), $k-\omega$ turbulent model (Yu et al. 2016; Zhou et al. 2018). Due to riblet micro-dimensions models such as Large-Eddy Simulation (LES) and Direct Numerical Simulation (DNS) have been found to be more capable to capture drag reduction mechanism (Chu and Karniadakis 1993; Duan and Choudhari 2014; Boomsma and Sotiropoulos 2016; Park and Choi 2017; Zhou et al. 2018; Al-Kayiem et al. 2020; Li 2020; Mele et al. 2020a,b; Zhang et al. 2020; Zhou et al. 2020).

The focus of this paper is merely to propose the new riblet configuration, hybrid configuration, which is able to apply to aircraft structure to reduce fuel consumption. Effects of different riblet configurations and arrangements on flow structure

and drag reduction studied using LES model. Three riblet configurations: sawtooth, scalloped, and hybrid, using two different arrangements: parallel and C-D were applied on both flat plate and NACA 0012 airfoil. Geometrical characteristics of three riblet configurations and numerical set-up were provided in the following section. A brief review of drag reduction mechanism was discussed and the results compared with previous works to select the optimized configuration.

2. GEOMETRICAL CHARACTERISTICS

2.1 Riblets Geometry

Riblet's spacing (s) and height (h) are important parameters that were used to compare different designs and define the flow conditions, which are shown in Fig. 1. These parameters are non-dimensionalised by the wall shear stress velocity and denoted by the superscript+; defined as following:

$$h^+ = \sqrt{C_f/2}\,(hU_\infty/\nu) = (hV_\tau/\nu) \tag{1}$$

$$s^+ = \sqrt{C_f/2}\,(sU_\infty/\nu) = (sV_\tau/\nu) \tag{2}$$

where C_f, U_∞ and ν are skin friction coefficient, freestream velocity and kinematic viscosity, respectively. V_τ is defined as wall shear stress velocity. Wall shear stress velocity or friction velocity is a form by which a shear stress is written in unit of velocity:

$$V_\tau = \sqrt{\tau_0/\rho} \tag{3}$$

where ρ is the fluid mass density and τ_0 is wall shear stress, which can be calculated from:

$$\tau_0 = \rho U_\infty^2 C_f/2 \tag{4}$$

Comparing Eq. (4) with Eqs. (1) and (2) shows the direct effect of non-dimensional geometrical parameters on skin friction. The non-dimensional riblet spacing and height find on shark scales lie in the range of $8<s^+<18$ and $8<h^+<10$, respectively.

Riblet dimensions were calculated based on the optimal non-dimensional height and spacing shown in the studies of Walsh (1983) and Caram and Ahmed (1991) along with the flow parameters at the selected Reynolds number to ensure an easy and accurate creation of both geometries and computational grids. The non-dimensional and actual riblet dimensions for the flat plate and airfoil cases are presented in Table 1. The non-dimensional riblet dimensions were forced to be fixed for all cases.

(a) Sawtooth riblet configuration

(b) Scalloped riblet configuration
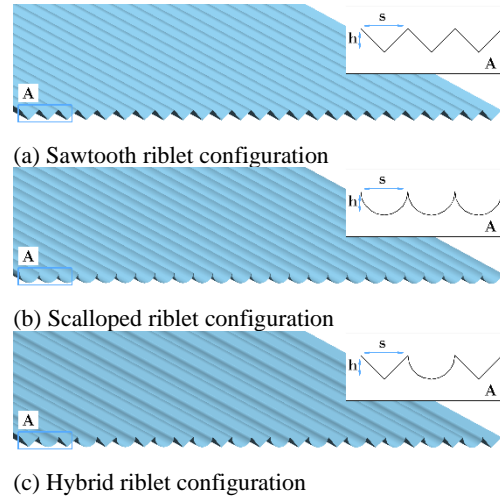

(c) Hybrid riblet configuration

Fig. 1. Three different riblet configurations. (a) Sawtooth configuration (b) Scalloped configuration. (c) Hybrid riblet configuration proposed by the current study to achieve improved performance over the original shape. The configuration was generated through placing the valley shape resulting between each sawtooth consecutive riblets between two semi-circular scalloped riblets. Close up A indicates the riblet spacing *s* and height *h* where *s=2h*.

To select an optimum riblet configuration, which contributes to maximum drag reduction, three riblet configurations were applied on a flat plate. These configurations were sawtooth, scalloped, and a new design called hybrid, which was a combination of sawtooth and scalloped. Figure 1 shows three riblet configurations. The close-up zone "**A**", indicates the riblet dimensions of spacing *s* and height *h*. The dimensions were based on the previous study since they provided favourable effects on skin friction reduction. Hence, the riblet spacing was selected to be double of the height or $s = 2h$.

The hybrid configuration was generated through placing the valley pattern resulting in each sawtooth consecutive riblets between two semi-circular scalloped riblets; which was an entirely unique configuration that was never previously studied. Subsequently, the optimum riblet configuration was applied on NACA 0012 airfoil with two different arrangements, parallel and C-D arrangements.

The dimensions were kept the same based on Reynolds number (Re) of 30'000 and non-dimensional spacing and height of 16 and 8, respectively, those parameters generated favourable results.

2.2 Flat Plate Geometry

Figure 2 displays dimensions of the flat plate, in terms of the riblet spacing "s". Due to the change in the geometric parameters selected for Re, the resulting calculated flow speed affected the relevant friction speed which in-turn affected the riblet dimensions.
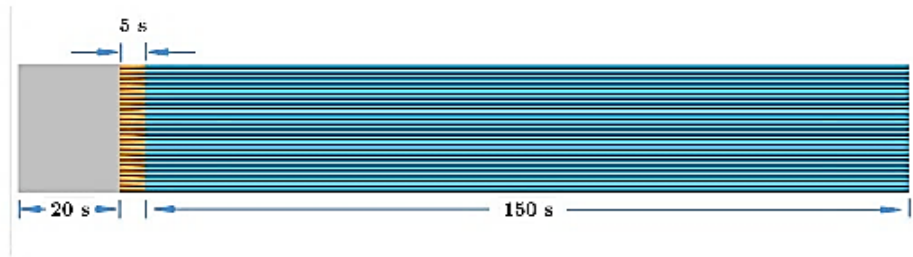
Table 1. Flat plate and airfoil riblet dimensions

Parameter	Flat Plate		NACA0012 Airfoil	
	Value	Unit	Value	Unit
s	2	*mm*	1.5	*mm*
h	1	*mm*	0.75	*mm*
s^+	16.38	-	16.38	-
h^+	8.19	-	8.19	-

Fig. 2. Flat plate dimensions used in the present study. The dimensions are provided in terms of non-dimensional riblet spacing, *s*. The actual flat plate is coloured with blue shade, the orange part acts as a leading edge blending from straight to riblet configuration, while the grey part is not considered a part of the plate.
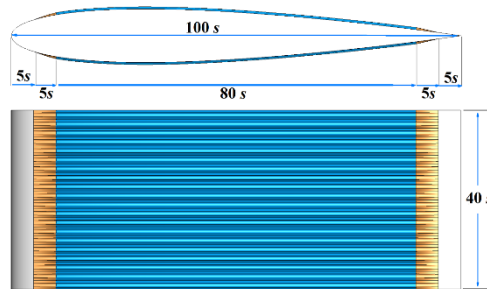

Fig. 3. NACA 0012 airfoil dimensions equipped with hybrid riblets. The dimensions were based on overall airfoil chord length of 0.15 m. Provided dimensions on the figure are presented with respect to the riblet spacing parameter *s*. Riblets applied to both upper and lower surfaces of the airfoil.
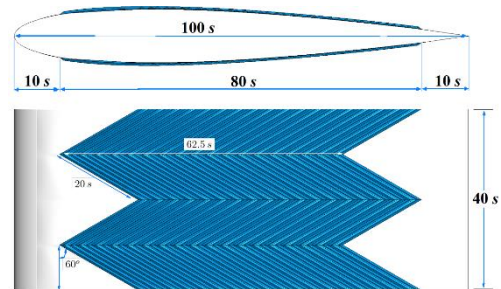

Fig. 4. NACA 0012 airfoil dimensions with C-D arrangement. All dimensions are with respect to the riblet spacing parameter *s*. The C-D riblet arrangement applied to both upper and lower surfaces of the airfoil.

In Fig. 2 the actual flat plate is coloured with blue shade, the orange part, titled buffer zone, acts as a leading edge blending from straight to Riblet configuration, while the grey part is not considered a part of the plate. The buffer zone in the boundary condition section, facilitated the grid elements from straight to riblet configuration. Moreover, the existence of this zone allowed for smooth transition of the flow over the plate rather than encountering sharp protrusions that induced immediate separation. The width of the plate was 25s, in which 25 riblet patterns existed.

2.3 Airfoil Geometry

Parallel Arrangement

The hybrid riblet configuration applied on the NACA 0012 airfoil with parallel arrangement, similar to the flat plate is shown in Fig. 3. The figure shows dimensions of the NACA 0012 airfoil with riblets applied to both upper and lower surfaces and the riblet locations. Since the actual chord length of the model was 0.15 *m*, this led to an overall non-dimensional length of 100*s*, while 80% of the airfoil surface was covered with riblets with 10% transition regions and 10% smooth surfaces. The width of the airfoil was 40*s*, in which 40 riblet patterns existed.

The reader might wonder why surfaces of the airfoil were not covered 100% with riblets; the reason is to avoid inducing turbulence or early separation at the leading edge, as well as improving the grid quality at both leading and trailing edges. In addition, a fully covered airfoil would not be feasible in real-life applications.

Convergent-Divergent Arrangement

Figure 4 shows the new riblet arrangement, which was applied on airfoil surfaces. The arrangement is C-D with two diverging lines and a single converging line running through middle planes. This arrangement was inspired by the experimental work of Xu *et al.* (2018).

The total number of riblet patterns on the surface in C-D arrangement were 36, which was reduced compare to parallel arrangement. This was due to geometry creation and modification for clean grid generation process. In this arrangement the riblet configurations were not directly aligned with the flow, whether parallel or perpendicular; they were in fact at an angle stated in Fig. 4. This was a result of the method by which the patterns were swept across the surface to produce the C-D arrangement.

The selected airfoil, NACA 0012, and Reynolds number of 30'000 based on the chord length were remained the same for both cases. Actual dimensions of the riblets were kept at solid numbers, which was a strategy followed in the parallel arrangement case to ensure an easy and accurate creation of both geometries and computational grids. The riblet dimensions were kept constant with the actual dimension and their non-dimensional counterparts, presented in Table 1.

Figure 4 shows that the angle at which the patterns arranged is $60°$. This angle is known as the yaw angle γ and selected based on the experimental work of Xu *et al.* (2018). Additionally, due to the riblet's pattern on the surface, the overall area covered by the C-D arrangement was 62.5%, which was a reduction from the previous case, 80%. The same cleared regions ahead and after the riblets of distance 10s were kept the same based on the work done previously, however no transition regions were necessary for this case.

It is worth mentioning that airfoil surfaces were not covered 100% with riblets, and the riblets were arranged in a zigzag manner with a defined beginning and end in chord-wise direction resulting in certain empty triangular regions in front and rear part of the airfoil. This was done solely for grid generation purposes and it will be explained in depth in the following grid generation section.

3. GRID GENERATION

Pointwise V18.0 R04 was used to generate a high quality grid to capture the physics of the problem. This is a dedicated grid generation software that enables users to generate high quality grids in relatively short period of time. However, the small size of riblets made the numerical study very expensive and due to the limitation of computational resources, an initial preferable grid was modified, and a finer mesh could not be used.

3.1 Riblets Grid Details

Figure 5 displays the hybrid riblet grid at the final generated step of the translation process and essentially shows the domain outlet as an example. Close-up **A** shows the fine grid generation approach taken in the generation of the grids. The aim was to satisfy the requirements of the accurate RANS SST $k - \omega$ model as well as LES approach with non-dimensional first layer thickness (y^+) of 0.1. Close-up **B** on the other hand shows the acute angle elements were generated between each riblet, which if left unchecked or untreated would lead to convergence limitations.

It is worth mentioning that for each riblet a total of 10 cells, or 11 grid points were used to capture the flow physics, result in 250 cells or 251 grid points for all grids in horizontal direction.
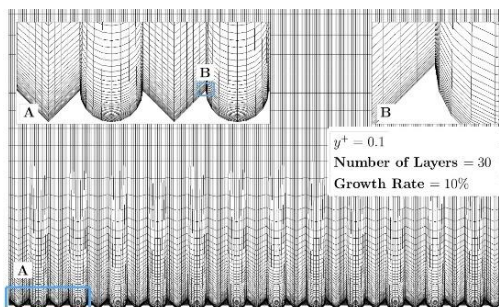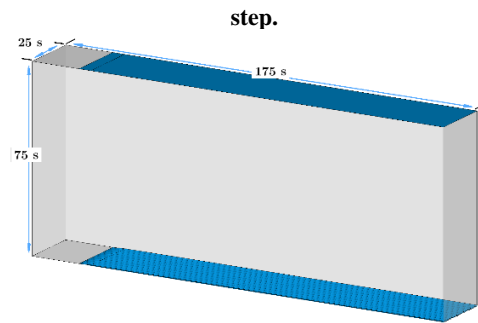

Fig. 5. Hybrid riblet grid at the last translated

Fig. 6. Dimensions of the overall domain created for flat plate studies.

Table 2 Flat plate viscous layer parameters

Parameter	Value	Unit
Re	30000	-
D_h	0.3	m
V	1.46	m/s
y^+	0.1	-
Δs	1.22×10^{-5}	m

3.2 Flat Plate Grid Details

The grid domain selected for the flat plate shows in Fig. 6 and dimensions of the domain are presented with respect to the riblet spacing parameter. It should be noted that the upper plate shown in blue region is considered as a smooth plate for all cases. The non-dimensional first layer thickness was assumed as 0.1 using information provided in Table 2; whereas the dimensional first layer thickness Δs obtained from the y^+ calculator provided from Pointwise software is equal to $1.22 \times 10^{-5}m$. Since the flat plate was considered inside a rectangular duct of length of 175s and width of 25s, the provided length parameter was selected as the hydraulic diameter D_h. Although the overall width that the hydraulic diameter was based on, is equal to the height at 175s, the symmetry property was considered assuming perfectly frictionless side walls, which allowed for dividing the domain into 3 parts and considering the third part only for simplicity and computational resources conservations.

A total of 4 different grids were generated for the flat plate case. The first one, a smooth flat plate, was set as a reference case for all studied cases. Then three different configurations on the plate: sawtooth, scalloped, hybrid. Grid parameters for all 4 cases were implemented to study the flat plate, including total of 9 blocks, 11,550,000 cells and 11,711,409 points. The flat plate grid topology is illustrated in Fig. 7. The total manually constructed block were 6, with the remainder 3 blocks generated automatically using the translation tool on Pointwise. The domain was split to lower, mid, and top groups to improve the overall grid quality. The translation was made such that the flat plate is 0.3 m long with 0.001 m width for each cell.

3.3 Airfoil Grid Details

The overall domain generated for the airfoil study is presented in Fig. 8. All dimensions of the C-Shaped
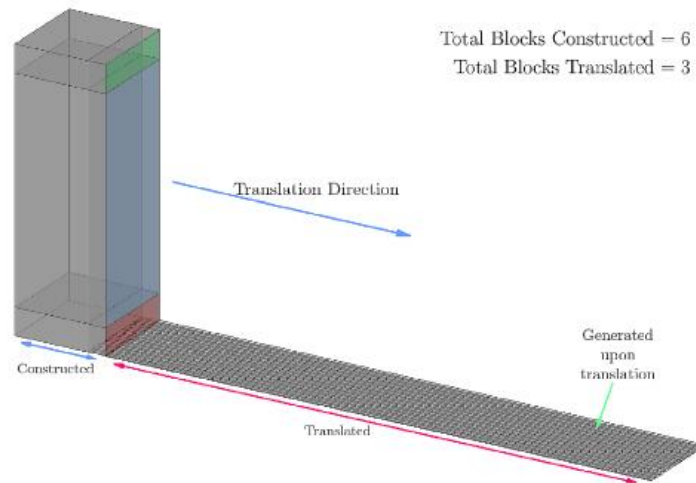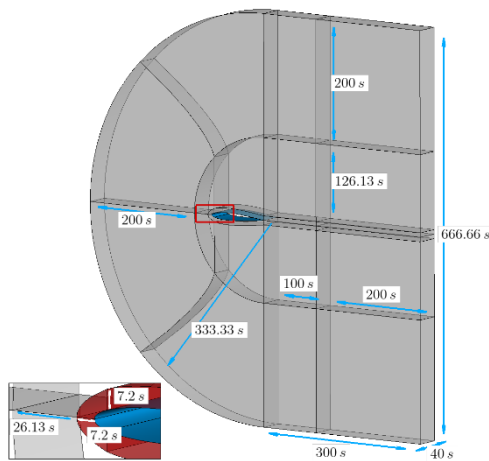
Fig. 7. Flat plate grid topology.

Fig. 8. Dimensions of the overall domain created for airfoil studies.

domain with respect to the riblet spacing parameters can be seen in the Fig. 8. Due to the complexity of the geometry, 24 blocks were generated in the solution domain.

The highlighted block shown in red represents airfoil viscous layer block. The airfoil viscous layer parameters were calculated similar to the flat plate case. The non-dimensional first layer thickness remains constant between the flat plate and airfoil cases to ensure the performance measurements in flat plate case, are replicated with no variation for the airfoil case. Summary of the airfoil viscous layer parameters are provided in Table 3.

A total of 6 different grids were generated for the airfoil case. The first one, a smooth airfoil, was set as

Table 3 Airfoil viscous layer parameters.

Parameter	Value	Unit
Re	30000	-
D_h	0.3	m
V	2.92	m/s
y^+	0.1	-
Δs	1.22×10^{-5}	m

a reference case for all studied cases. The next three were for parallel arrangement study including sawtooth, scalloped, and hybrid configuration. The last two C-D arrangement study including hybrid configuration applied on the upper surface and hybrid configuration applied on both surfaces. Grid parameters for all 6 cases were implemented to study the airfoil, including total of 24 blocks, 16,240,000 cells and 16,497,140 points.

4. NUMERICAL SETUP

4.1 Flat Plate Setup

SST $k - \omega$ was selected as a turbulence model with low Reynolds number correction option enabled in order to account for the relatively low Reynolds number of the case. The air fluid parameters of density and dynamic viscosity were set as standard sea-level conditions.

It is very important to specify correct turbulence parameters at the inlet as it determines how close the averaged obtained results are to real life. The turbulent intensity and length scale parameters were calculated based on the Reynolds number and boundary layer thickness (δ): I = 0.16 $Re^{-1/8}$ and $l = 0.4\delta$, respectively. The Second Order Up-wind was selected as the discretisation scheme and to calculate the gradient across the cells, Least Squares Cell Based method was used due to its accuracy and relatively low-cost. Table 4 states the values specified in the set-up step for the flat plate.

4.2 Airfoil Setup

The simulation set-up remained unchanged for all cases as stated previously. The simulations were done in two stages, initializing steady state stage using SST $k - \omega$ RANS model for 1000 iterations, followed by the higher fidelity LES approach based on Wall-Adapting Local Eddy-viscosity (WALE) as recommended by ANSYS Fluent for a total of 1500 time steps, out of which 1000 were averaged and presented in the study. Table 5 displays a summary

Table 4 Set-up parameters used for study the flat plate.

Parameter	Value
Velocity	1.46 (m/s)
Turbulent Intensity	4.41042%
Turbulent Length-scale	0.00565 (m)
Gradient	Least Squares Cell Based
Pressure	Second Order
Momentum	Second Order Upwind
Turbulent Kinetic Energy	Second Order Upwind
Specific Turbulence Dissipation Rate	Second Order Upwind

Table 5 Simulation stages of airfoil studies .

Stage 1	Steady State RANS	SRANS
Stage 2	Large Eddy Simulation	LES

of the stages alongside the approach selected for each stage.

Steady State Stage:

This stage deployed steady RANS SST $k - \omega$ model to initialize the flow prior to starting the higher fidelity calculations. The low Reynolds treatment option was activated since the Re of the problem was relatively low. It is important to mention that the problem was considered to be fully incompressible in nature and the specified flow properties set as standard condition. Inlet boundary conditions are tabulated in Table 6.

The discretisation of all governing and transport equations were performed using the Second Order Upwind scheme. This scheme is very stable and produces favourable results for external aerodynamic studies. In addition, Least Squares Cell Based method was deployed to calculate the solution gradients across the cell faces. These methods are low-cost and have the least possible impact on the computational resources while maintaining an acceptable level of accuracy.

Since the problem falls within the incompressible flow regime using of pressure-velocity coupling method is recommended. The steady part of the solution provided an accurate initialised flow for the LES part of the calculations. The selected algorithm

hence was Coupled. This algorithm is more accurate than a predictor corrector method such as SIMPLE and its family, and it is generally favoured for aerodynamic CFD studies.

Table 6 Flat plate inlet boundary condition details.

Parameter	Value	Unit
Velocity	2.92082	*m/s*
Angle of attack	6	*deg*
Turbulent Intensity	4.41042	*%*
Turbulent Length-scale	0.00282	*m*

Table 7 Time-stepping information of LES studies.

Parameter	Value
Time step size	0.0005 sec
Overall time	0.75 sec
Total time steps	1500
Transition stage	500
Statistics stage	1000
Total flow passes	14.6

Unsteady Stage:

When the turbulence approach was switch to the LES, Fluent automatically adjusts the solution time to be transient instead of the original steady. This is due to the fact that LES can only be carried out with respect to time and hence it cannot be constant. Thereafter, it would be possible to modify the schemes by which time can be discretised. Selected scheme was Bounded Second Order Implicit, which is the most accurate scheme available within the solver and it is of an equivalent order of accuracy with all other transport equations. Additionally, LES should only be carried out using Bounded Central Differencing scheme for momentum transport equation.

Another important change with the second stage of the solution was the pressure-velocity coupling method. At this stage the non-iterative approach was selected to allow the progression of the solution in time without solving iterations in pseudo-steady state. This approach saved 20 to 30 inner iterations per single time step. The non-iterative method of choice was Fractional Step. This method dramatically cuts the required real-life simulation time, which is already high enough due to the fact that LES directly solves significant portion of the flow without modelling.

Table 7 summaries main parameters used to run the calculations of the second-high fidelity stage of the simulations. It can be seen that a total of 500 time steps with size of 0.0005 seconds were dedicated towards transitioning the flow from the steady state flow field to a fully initialised transient flow field.

5. RESULTS AND DISCUSSION

In this section, numerical results of aerodynamic performance *i.e.* lift, drag, and skin friction coefficients of a flat plate and NACA 0012 airfoil presented in order to understand the effect of the parallel and C-D riblet arrangements on the macro scale.

5.1 Flat Plate

Skin Friction Coefficient Analysis

A preliminary study was conducted on the flat plate geometry with different riblet configurations: sawtooth, scalloped and the new proposed hybrid design. Smooth flat plate was used as a reference case. All riblet configurations were compared with the smooth flat plate to determine their effectiveness.

Table 8 Flat plate skin friction coefficient reduction in percentage.

Flat plate surface	C_f	Reduction (%)
Smooth	0.00733387	-
Sawtooth riblets	0.00722187	1.53%
Scalloped riblets	0.0064524	12.02%
Hybrid riblets	0.00629938	14.11%

Table 8 summaries the results of total skin friction coefficient (C_f) and Fig. 9 represents the skin friction coefficient distribution over the flat plate surface with three different riblet configurations (sawtooth, scalloped, and hybrid). Skin friction coefficient is non-dimensionalised skin friction drag, which is a drag produces by the friction between fluid and solid surface. Table 8 shows total skin friction coefficient reduction in sawtooth configuration is only 1.53%. The distribution in Fig. 9 shows sawtooth configuration is not as effective as other configurations, when the flow becomes turbulent towards the leading edge (x/L>0.6). However, the total skin friction improvement increases to 12.02% and 14.11% in scalloped and hybrid riblet configurations, respectively. The skin friction distribution is the least for the hybrid configuration (Fig. 9), as this riblet configuration reduces the flow contact area and decreases the wetted area by pushing up the vortices in turbulent flow. Moving away the vortices results in reducing the shear stress and decreasing the skin friction coefficient.

In addition, it can be seen that there is a gradual increase in C_f for the smooth plate and sawtooth configuration towards the trailing edge. There is 53.9% increase occurs between 0.5<x/L<0.7 for smooth plate and 73.3% increase between 0.62<x/L<0.8 on the sawtooth plate. For both cases C_f remains constant after this increment. The increment occurs due to flow transition from laminar to turbulent near the surface of the plate. In contradiction, in the scalloped and hybrid

configurations, C_f continuously decreases along the total length of the plate, which indicates that reducing skin friction by moving the turbulent eddy vortices is stronger. This proves that the effectiveness of the sawtooth configuration is less compare to the other two modifications in decreasing the skin friction coefficient.

In addition, maximum averaged wall shear stress was also reduced by applying riblet structures (results not shown in the paper). The main factor in reducing surface shear stress is reducing velocity gradient close to the wall; by pushing the vortex away from the surface and decreasing the contact surface area and velocity gradient close to the wall. The maximum value of averaged wall shear stress by applying riblet structures happened on apexes of each riblet at the leading edge, reduced as moving towards the riblet's valley and as moving towards the trailing edge on the apexes.

Boundary Layer Properties

Figure 10 represents the flat plate velocity profile for all configurations; smooth, sawtooth, scalloped and hybrid. It is shown that the smooth plate has the highest velocity gradient in the vicinity of the wall and turbulent effect compared to the flat plate with riblet modifications. Higher velocity gradient next to the wall is due to the present of large eddies, which leads to higher shear stress at wall. The highest velocity gradient belongs to the smooth surface followed by the sawtooth riblet configuration. The difference between these two cases is negligible and can be concluded that the sawtooth riblet has the least effect on transferring the turbulent vortices away from the wall. This transformation is more effective in hybrid and scalloped configurations. The velocity gradient within an approximate linear region next to the wall decreases 54% and 110.5% in hybrid and scalloped configurations, respectively.
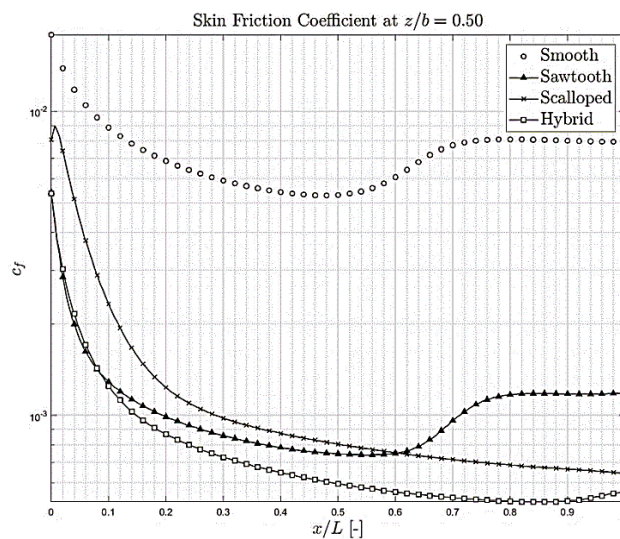

Fig. 9. Skin friction coefficient, C_f, of the flat plate for four different configurations: smooth, sawtooth, scalloped, and hybrid configurations. The data was extracted at z/b=0.5, which is at mid-plane.
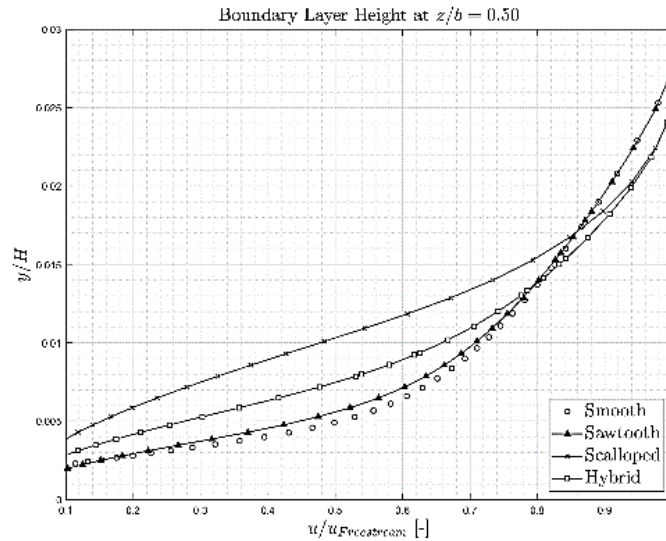
Fig. 10. Boundary layer velocity profile of the smooth flat plate and the plate with three riblet modifications: sawtooth, scalloped, and hybrid.
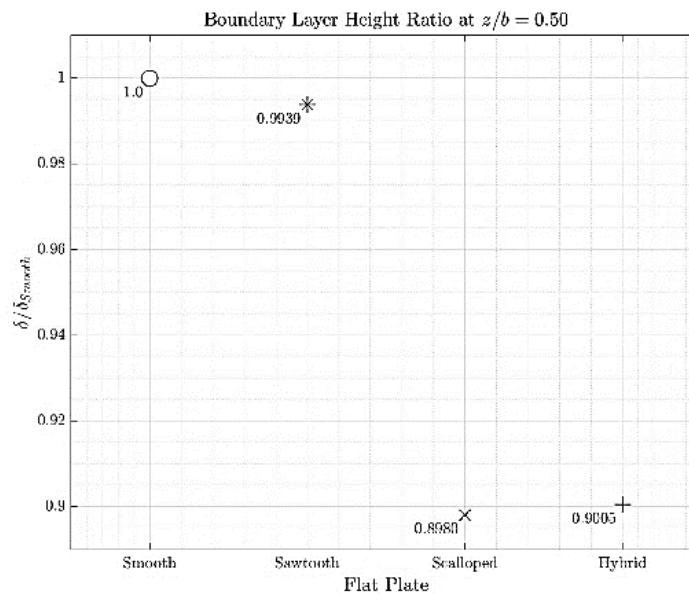

Fig. 11. Dimensionless boundary layer height for sawtooth, scalloped, and hybrid configurations at x/c=0.5.

For the riblet surface, especially hybrid and scalloped configurations, it was noticed that the viscous sublayer thickness increased in comparison to smooth surface, due to the distance created between the streamwise vortex and the wall by the riblets. It is also noticed that the increase of viscous sublayer thickness made a buffer region and the logarithmic region moved upwards. Thus, the velocity at the same position was decreased in comparison with the smooth surface; leading to the drag reduction.
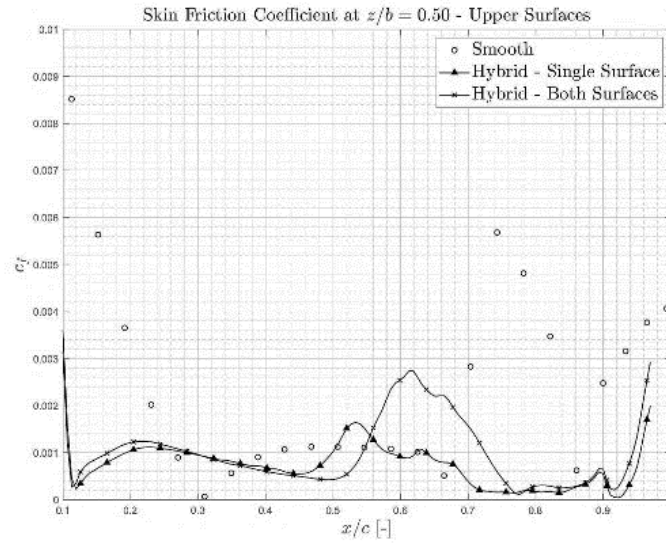
The dimensionless boundary layer thickness (δ/δ_{smooth}) was also compared between all studied cases and is shown in Fig. 11. The thickness of boundary layer in sawtooth configuration is almost same as the smooth plate. This emphasises on containing larger and stronger eddy structures inside

the boundary layer result in greater velocity gradients near the wall, hence higher wall shear stress. Boundary layer thickness in scalloped and hybrid configurations is almost the same with a sharp drop compared to the smooth plate, by 90% reduction in their height.
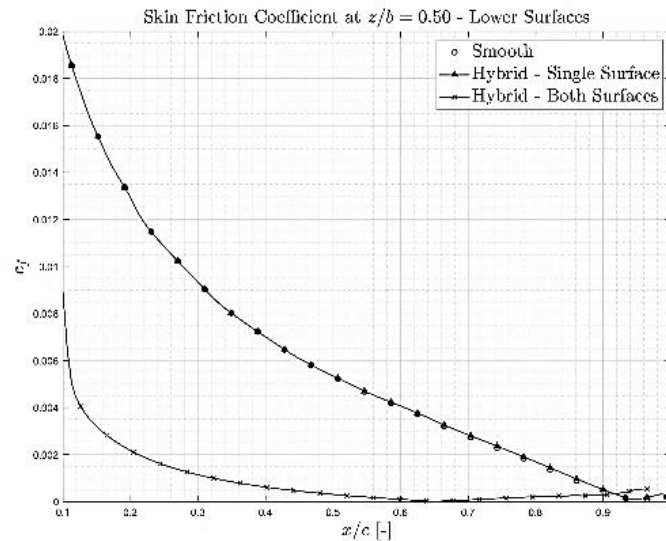
5.2 NACA 0012 Airfoil – Parallel Arrangement

Skin Friction (C_f) Analysis

Since the new proposed riblet design, hybrid configuration, achieved the highest skin friction drag reduction on flat plate, hybrid riblet configuration was applied on NACA 0012 airfoil. There were two different dispositions for the airfoil surface: partially

(a) C_f on the upper surface

(b) C_f on the lower surface

Fig. 12. Skin friction drag coefficient on the (a) upper surface and (b) lower surface of the NACA 0012 airfoil for three different arrangements.

Table 9 Airfoil skin friction coefficient reduction in percentage with hybrid riblet configuration applied partially and fully to NACA0012

Airfoil surface	C_f	Reduction (%)
Smooth	0.016007	-
Partial riblets	0.011726	26.7%
Fully riblets	0.010489	34.5%

disposition, which riblets applied only on the upper surface of the airfoil and fully disposition, which riblets applied on both upper and lower surfaces.

Table 9 summarised effect of two dispositions on airfoil total skin friction coefficient. The total skin friction coefficient decreases 26.7% in partially disposition compare to the smooth airfoil, while this

reduction will increase to 34.5% in fully disposition. The reason of this reduction discovered by plotting skin friction coefficient distribution on the upper and lower surface of the airfoil NACA 0012 in Fig. 12.

On the upper surface, Fig. 12a, the smooth surface has the highest friction coefficient near the leading edge with a value of 0.0085, which decreases rapidly to 0.0005 at 30% of the chord. It remains approximately constant until 65% of the chord when increases once closer to the trailing edge. In contrast, both hybrid configurations show a much lower value of C_f. There is a bell shape peak in both dispositions between 50% and 75% of the chord due to the formation of a flow separation bubble, where wall shear stress is increasing (see Fig. 12a). The rise in the skin friction coefficient value at the region close to the trailing edge for all three arrangements is due to the mixing of the vortices from the bottom surface,
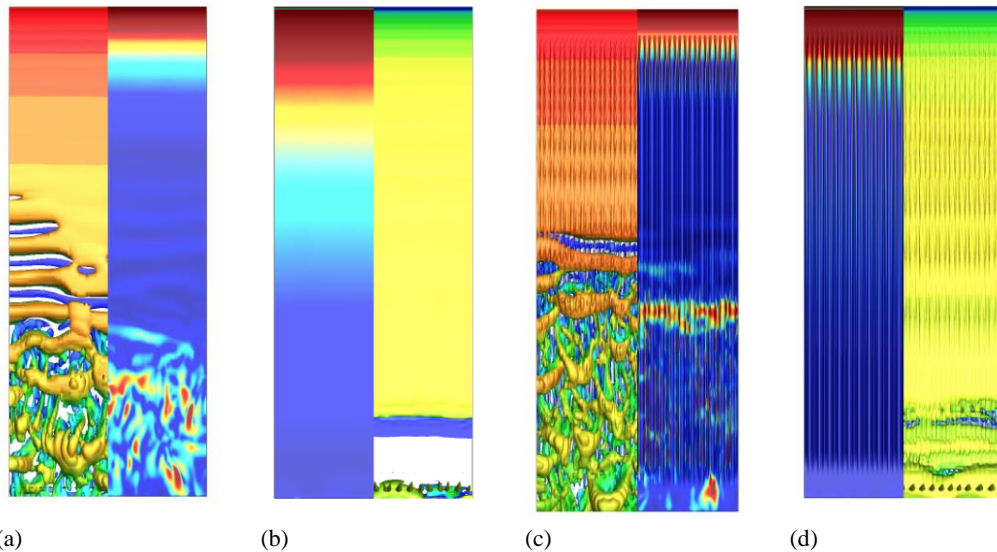
(a) (b) (c) (d)

Fig. 13. Q-Criterion contour on the left and skin friction coefficient on the right over upper and lower surfaces of the airfoil. The contours provided for two different dispositions: smooth and fully hybrid disposition. Flow direction is from top to bottom. (a) Smooth airfoil – Upper surface (b) Smooth airfoil - Lower surface (c) Fully hybrid disposition - Upper surface (d) Fully hybrid disposition - Lower surface.

however, the peak is lower by applying riblet modification on the airfoil surface.

On the lower surface of the airfoil, Fig. 12b, the smooth and partially riblet disposition are the same trend, as the lower surface of these airfoils were the same being riblet-less and smooth. For the airfoil with hybrid riblets on the lower surface, a significant difference can be seen. Skin friction more rapidly decreases from the leading edge all the way towards the trailing edge. This is due to the continuously attaching flow presenting effective drag reduction characteristics.

Vortices & Q-Criterion

To better understanding of the vortical structure over the airfoil the Q-criterion has been calculated for the flow field. The Q-criterion is the second invariants of the velocity gradient tensor, which is presented by Eq. 5:

$$Q = \frac{1}{2}\left[\left(tr(\nabla u)\right)^2 - tr(\nabla u)(\nabla u)\right] \qquad (5)$$

Q iso-surface is a good indicator of turbulent flow structures. Fig. 13 compares vortical structure on upper and lower surfaces of the smooth and fully hybrid disposition airfoils using Q-Criterion contours. Each subfigure contains two contours Q-Criterion contour on the left and C_f contour on the right.

The separation onset is earlier with the riblet fitted surface, which is consistence with the formation of larger eddy covered region on the surface (Figs. 13a compare to 13c). Additionally, the actual shear stress acting on the surface is drastically decreased in both attached and separated regions on the airfoil surface equipped with the riblet modification. Initially, in the attached region, the shear contours are much higher

and more intense for the smooth airfoil. This is carried forward to the separation region where the eddies interact more with the smooth airfoil than the riblet arrangement airfoil, with the exception of the first separation bubble which remains attached to the surface for a short distance and afterwards breaks down quickly. It should be highlighted that the riblet surface has more eddies due to the earlier separation yet experiences less skin friction drag.

On the lower surfaces, Figs. 13b & 13d, the entire airfoil lower surface equipped with riblets experiences less skin friction than the smooth one starting from the leading edge to the trailing edge, without experiencing separation due to the orientation with respect to the flow direction. Some irregularities are seen towards the trailing edge, which occurs due to the effect of the separated flow and the wake being dragged behind the airfoil.

5.3 NACA 0012 Airfoil – C-D Arrangement

Skin Friction (C_f) Analysis

The C-D arrangement, Fig. 14, was studied using hybrid and sawtooth riblet configurations applied to the upper and lower surfaces of the airfoil. away from the surface is more effective compare to other riblets configurations.
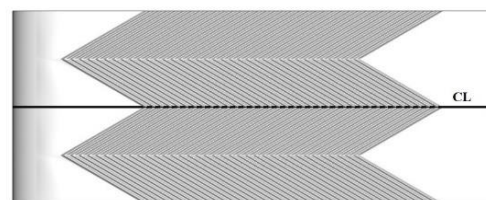

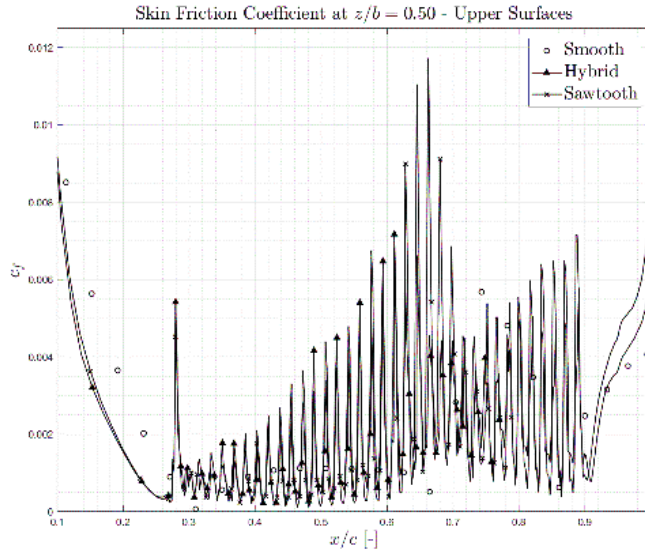**Fig. 14. C-D arrangement. Converging line (CL) location is shown with a bold line.**

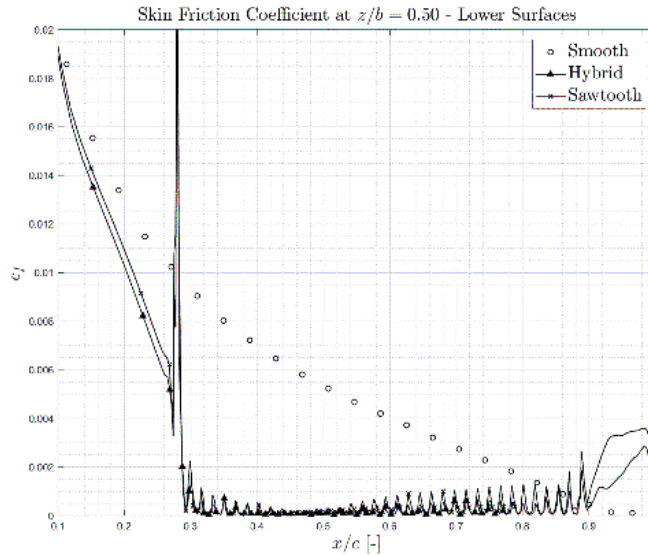**Fig. 15. Upper surface skin friction at Converging line (CL)**

Fig. 16. Lower surface skin friction at Converging line (CL).

Table 10 Skin friction coefficient reduction in percentage for the C-D arrangement.

Airfoil Surface	C_f Reduction (%)
Smooth	-
Sawtooth Riblets	26.75%
Hybrid Riblets	34.5%

Table 10 summarises the total skin friction coefficient reduction. Same as the results for the parallel arrangement the most reduction belongs to the hybrid riblet configuration with 34.5% decrease compare to the smooth airfoil. It can be concluded that the hybrid riblet configuration function in pushing the vortices

The data showed in this section was extracted at the centerline of the airfoil, called Converging Line, CL, at z/b=0.50, since the flow at this region is smoother and its behaviour can be easier identified.
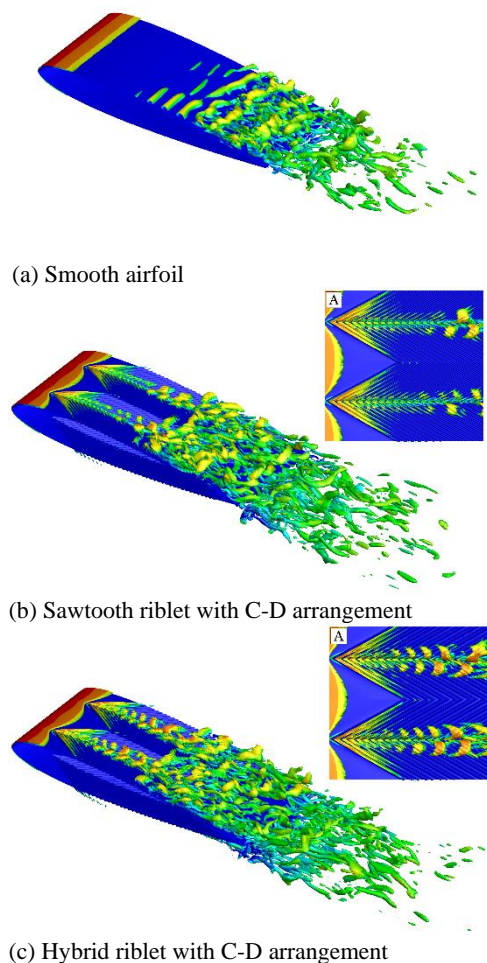
Figure 15 represents the airfoil upper surface skin friction coefficient distribution along the converging line at z/b=0.50. By applying the modification, the skin friction experiences smooth decrease from 0.009 at x/c=0.1 to approximately 0.0005 at x/c=0.27, which represents the smooth area before the converging line. After x/c=0.27, the flow will cross over the riblets, which are aligned with a yaw angle. Skin friction experiences oscillatory changes, which continues until x/c=0.9 at end of riblet section. These oscillations are created due to interaction between the crossflow and the axial flow along the riblet's valley generates a secondary flow inside the valley in a helicoidal motion pattern. These secondary helicoidal flows collide over the converging line and create oscillations in shear stress and skin friction coefficient.

Figure 16 represents the airfoil lower surface skin friction distribution along the converging line. It is

observed that the skin friction coefficient starts to decrease from 0.019 to almost zero between x/c=0.1 and x/c=0.28 in the smooth region. At x/c=0.28 there is a dramatic increase in skin friction followed by an oscillation around zero value until the end of the riblet configuration at x/c=0.9. At x/c=0.9 there is a slight increase in the skin friction until the trailing edge.

Vortices & Q-Criterion

Vortical structure of flow with sawtooth and hybrid riblet configurations in C-D arrangement was illustrated in Fig. 17. The results show the C-D surface texture acts like a vortex generator, as the vortical structures start from the tip of the diverging regions and then they tend to flow together along the airfoil when they reach at the converging line of the C-D surface, allowing the airflow in the boundary layer to withstand the adverse pressure gradient longer, unlike the airfoil with smooth surface where the vortical structures start from the middle of the

(a) Smooth airfoil

(b) Sawtooth riblet with C-D arrangement

(c) Hybrid riblet with C-D arrangement

Fig. 17. Isometric view of Instantaneous velocity distribution on smooth and textured airfoils (a) Smooth Airfoil (b) C-D surface airfoil with sawtooth riblets (c) C-D surface airfoil with hybrid riblets.

airfoil surface. It is clear that the vortical structures with hybrid riblets start earlier at the tips of the diverging region than the ones with sawtooth riblets which further delays the boundary layer flow separation.
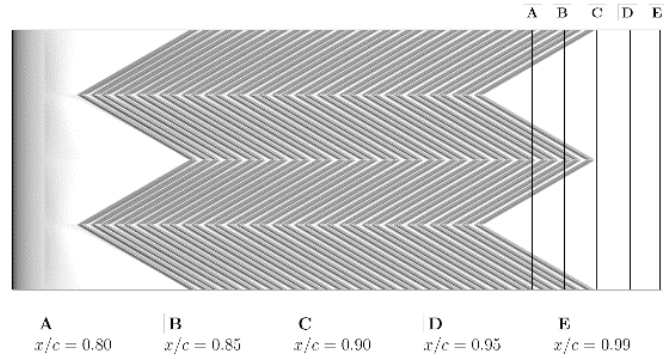
Spanwise Velocity Distribution

To illustrate the spanwise velocity variations, spanwise distribution of an induced streamwise velocity were plotted in Fig. 18 at five different locations, ranging from x/c=0.8 to x/c=0.99.

Over the diverging lines at z/b=0.25 and 0.75, both magnitude and width of the velocity excess increase. This excess increase can be seen until the end of the airfoil at x/c=0.99. However, the strength of this effect is gradually diminished as moving towards the end of the airfoil chord line. In contrast, the velocity magnitude reaches to the minimum value between the two peaks at diverging lines. This minimum value is almost flat and equal to zero at two locations, x/c=0.8 and 0.85, which are within the riblet decomposition. At other three x/c locations, the minimum velocity value is not zero. At z/b=0.25 it slightly increases to reach a plateau value and then slightly decreases back to its initial value as it reaches to the next diverging line at z/b=0.75. The spanwise velocity distribution indicates that the whole flow field is affected by the local upwash and downwash motion, which are formed by a weak recirculating secondary flow across the riblet section. An upwash motion dominates over the converging region, whereas the downwash motion dominates over the diverging region.
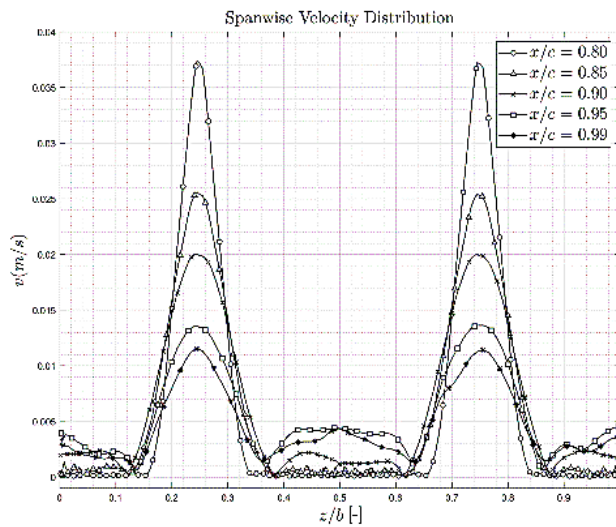
Vortex Shedding

Riblet modification on the airfoil had direct effect on vortex formation and vortex shedding. Figure 19 shows a backview of three different airfoils. The airfoil without a riblet modification (Fig. 19a) and two with hybrid riblet configuration, Fig. 19b using parallel arrangement and Fig. 19c using C-D arrangement. On the smooth airfoil vortices trap inside the wake of the airfoil and stay close to the surface. This attachment of vortices to the surface strengthens the shear stress experienced by the surface and increases the overall drag. Applying the riblet on the airfoil surface tends to reduce the skin friction drag by lifting up the vortices from surface. Both parallel and C-D arrangement have almost the same effect in lifting up the vortices on the upper surface of the airfoil. On average C-D arrangement pushes the vortices approximately 3% more compare to parallel arrangement. However, C-D configuration also has influence on the lower surface of the airfoil, by which the vortices are pushing away from the lower surface. This influence cannot be seen on neither the smooth surface nor parallel arrangement.

The flow on the lower surface of the C-D arrangement is more stable as the flow pattern is repeated between diverging and converging lines. It creates a downwash motion by the diverging line,
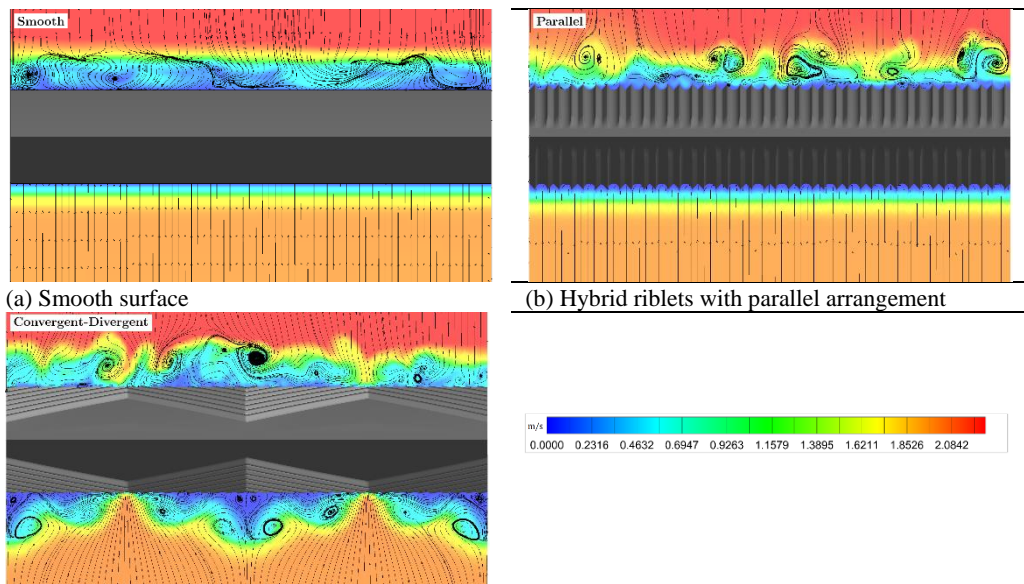
(a) Spanwise location

(b) Velocity distributions

Fig. 18. Spanwise velocity distributions at different longitudinal locations ranging between *x/c*=0.8-0.99. *z/b* is spanwise direction between 0 and 1. Converging line locates at mid-plane, *z/b*=0.5 and two diverging lines locate at *z/b*=0.25 and 0.75.

(a) Smooth surface

(b) Hybrid riblets with parallel arrangement

(c) Hybrid riblets with C-D arrangement

Fig. 19. Velocity distribution (m/s) around NACA 0012 airfoil. It shows Backview of the airfoil with and without hybrid riblet modifications using two different arrangements: (a) NACA 0012 with smooth surface, (b) NACA 0012 with hybrid riblet configuration - parallel arrangement, (c) NACA 0012 with hybrid riblet configuration - C-D arrangement. Figure shows velocity contour and streamlines on both surfaces.
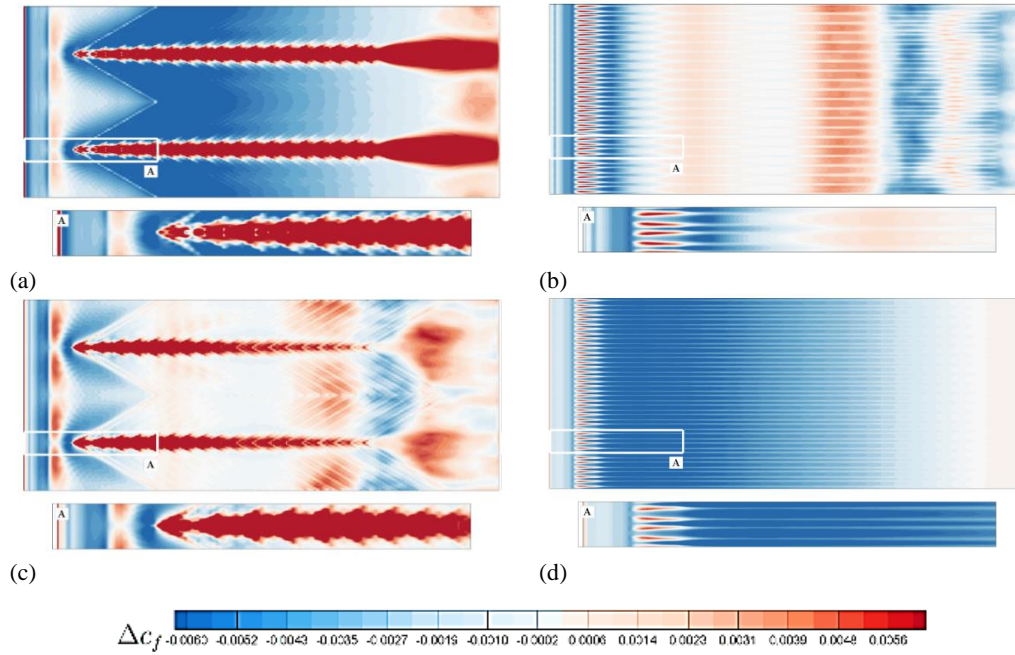
Fig. 20. Skin friction difference ΔC_f by adding C-D and parallel riblets arrangement to the top and bottom airfoil surfaces (a) C-D - Top surface (b) Parallel - Top surface (c) C-D - Bottom surface (d) Parallel - Bottom surface.

which the stagnation happens at the valley of the riblet. Then it moves towards the conversing line, while staying close to the surface. Interaction of this flow and the bulk flow induces a vortex in the vicinity of the surface. As the flow inside the riblet reaches close to the converging line, it mixes with the flow inside the neighbouring riblet arrangement and produces an upwash motion next to the converging line. Vortex which was created earlier moves away from the surface with the upwash motion, which causes reduction in skin friction drag.

Change in Skin Friction

Figure 20 shows the change in skin friction coefficient, ΔC_f due to applying hybrid riblet with C-D and parallel arrangement. The change in skin friction is defined as the following:

$$\Delta C_f = C_{f,riblet} - C_{f,smooth} \qquad (6)$$

Figure 20a indicates the top surface of the airfoil, which was equipped with C-D riblet arrangement. It shows the tip of the two diverging lines experience an increase in skin friction and lasts all the way to the end of the airfoil surface. This increase in the skin friction is due to a vortex generated at the tip of diverging line in the C-D arrangement. C-D riblet arrangement acts as a vortex generator on the surface, which causes the flow stays more attached to the surface and increases interaction between the vortices and the surface. However, the concentration of high skin friction is not dominant on the upper surface and the rest of the upper surface regions experience low skin friction; hence it compensates the increase along the diverging lines. Figure 20b indicates the skin friction coefficient using parallel arrangement. It shows a noticeable skin friction

reduction as the parallel riblet section begins on the upper surface. Afterwards, ΔC_f gradually increases until passing the mid chord section, which flow separation starts to form as shown previously in Fig. 13c.

Bottom surface of the airfoil experiences same trend as the upper surface, with concentration of skin friction coefficient along the diverging lines on C-D arrangement (Fig. 20c) and gradual increase in parallel arrangement (Fig. 20d).

5.4 Force Coefficients Analysis

Tables 9 and 10 show skin friction coefficient reduction of NACA 0012 by applying hybrid riblet configuration in C-D arrangement and parallel arrangement is the same, with total of 34.5% reduction in C_f. In order to compare parallel and C-D arrangements in more details, force coefficients and aerodynamic efficiency (L/D) of the NACA 0012 airfoil were obtained and presented in Table 11.

It can be seen that the lift coefficient, C_l, is increased with C-D arrangement by 8.33%. On the other hand, with the parallel arrangement the lift coefficient is decreased by 10%. The C-D arrangement has also advantage on drag reduction, as total drag coefficient, C_d, is decreased by 8.36%. With the parallel arrangement the total drag coefficient is increased by 32.85%.

The moment coefficient gives insight of the design stability, the lower the value of C_m, the more stable the design is, which can be seen with C-D riblet arrangement. Another important performance parameter of an aircraft is the lift to drag ratio or aerodynamic efficiency. The higher aerodynamic

Table 11 Force coefficient of smooth, parallel, and C-D arrangements on NACA 0012 airfoil with hybrid riblet configuration. (+) indicates increase in percentage, while (-) indicates decrease in percentage.

Force coefficient	Smooth	Parallel	C-D
C_l	0.4649	0.4179	0.5072
Percentage (%)	-	-10%	+8.33%
C_d	0.049	0.0651	0.0449
Percentage (%)	-	+32.58%	-8.36%
C_m	-1.0353	-0.9383	-1.136
Percentage (%)	-	+9.36%	-8.86%
L/D	9.48	6.42	11.29
Percentage (%)	-	-32.27%	+19%

efficiency, the better fuel economy in aircraft, climb performance, and glide ratio. The C-D arrangement produces the highest lift to drag ratio. Thus, it is more favourable than the parallel arrangement.

6. CONCLUSION

In this research numerical simulations were performed using LES to investigate the effect of using riblets on reducing skin friction drag. The drag reduction performance of a new riblet design called hybrid riblet configuration along with two other configurations: sawtooth and scalloped was studied. These configurations were applied on the surface of a flat plate and NACA 0012 airfoil using parallel and C-D arrangements. The key findings are summarised as follows:

Parallel Arrangement - Flat Plate: Among three configurations, hybrid riblet configuration with parallel arrangement had the most improvement effect on the flat plate by decreasing 14.11% of skin friction coefficient. Comparing the wall shear distribution showed that it decreased on the smooth flat plate initially and increased as the flow turned into turbulent flow on the surface. On the other hand, hybrid riblet configuration forced the wall shear stress to decrease after initial increment, all the way on the plate surface.

Parallel Arrangement – NACA 0012 Airfoil: The results for NACA 0012 were consistent with the flat plate with the highest skin friction reduction using hybrid riblet configuration. The reduction was 26.7% in partially deposition and 34.5% in fully deposition case. It was concluded that combination of aerodynamic body with the riblet modification reduced 89% more of the skin friction coefficient. This combination had more control on flow separation to localise the separation and led to decrease more skin friction coefficient.

C-D Arrangement – NACA 0012 Airfoil: Skin friction coefficient reduction by applying C-D arrangement and hybrid configuration to the airfoil was the same compare to the parallel arrangement,

total 34.5% reduction. In this regard, aerodynamic efficiency of the airfoil was investigated and found that lift coefficient decreased 10% and overall drag coefficient increased 32.85% in parallel arrangement, however, the lift coefficient increased 8.33% and overall drag coefficient decreased 8.36% in C-D arrangement. Therefore, aerodynamic efficiency of the airfoil increased 19% in C-D arrangement, however, reduced by 32.27% in parallel arrangement. The stability of the airfoil was also improved by adding the C-D hybrid arrangement as the moment coefficient C_m was reduced by 8.86%.

Spanwise velocity distributions in C-D arrangement agreed with the previous research and showed velocity peaks around the diverging line followed by a reduction close to the converging line.

Skin friction change ΔC_f contours obtained with the C-D arrangement and parallel arrangement proved that the C-D arrangement had better performance since the skin friction was more concentrated along the diverging line, smoothly increasing on the upper surface of the airfoil. The flow separation was delayed which improved the aerodynamic efficiency of the airfoil. On the other hand, parallel arrangement showed a gradual increase up to 68% of the chord followed flow separation and skin friction fluctuations; resulted in increasing the overall drag and reducing aerodynamic efficiency.

It was concluded that optimal drag reducing feature was the new design, hybrid configuration, with the lowest skin friction coefficient for the airfoil. This design can be applied on aircraft to improve the aerodynamic efficiency and reduce aircraft fuel consumption. In wild-body aircraft such as Airbus A380, A340 and Boeing 747, 777, weight of fuel and empty weight on average are 41%-45.7% and 50%-65% of maximum take-off weight, respectively (Wikipedia 2020). Reducing 1% of fuel weight would increase 0.7% of empty weight. In narrow-body aircraft, on average fuel weight is one-forth and empty weight is half of the maximum take-off weight. In these aircraft, reducing 1% of fuel weight would increase 0.5% of empty weight. This extra empty weight can be used for more passengers, which is on average 18-26 more passengers for wild-body aircraft and 3-4 more passengers for narrow-body aircraft or can be used for extra cargos, which is beneficial for the airliners.

Further studies such as experimental testing of flow behaviour around the airfoil equipped with hybrid riblet configuration and its wake region is recommended. For numerical studies, changing the geometry from two diverging lines to two converging lines may enhance the flow mechanism and obtain more effective results in drag reduction.

REFERENCES

Al-Kayiem, H. H., D. C. Lim and J. C. Kurnia (2020). Large eddy simulation of near-wall turbulent flow over streamlined riblet-structured surface for drag reduction in a

rectangular channel. *Thermal Science* 24(5 Part A), 2793-2808.

Aupoix, B., G. Pailhas and R. Houdeville (2012). Towards a general strategy to model riblet effects. *AIAA journal* 50(3), 708-716.

Bechert, D. W., M. Bruse, W. V. Hage, J. T. Van der Hoeven and G. Hoppe (1997) Experiments on drag-reducing surfaces and their optimization with an adjustable geometry. *Journal of Fluids Mechanics* 338, 59-87.

Bechert, D. W. and W. Hage (2006). Drag reduction with riblets in nature and engineering. *WIT Transactions on State-of-the-art in Science and Engineering* 4, 111-127.

Benschop, H. O. G. and W. P. Breugem (2017). Drag reduction by herringbone riblet texture in direct numerical simulations of turbulent channel flow. *Journal of Turbulence* 18(8), 717-759.

Bhushan, B. (2009). Biomimetics: lessons from nature– an overview. *Philosophical Transactions of the Royal Society A: Mathematical, Physical and Engineering Sciences* 367(1893), 1445-1486.

Bhushan, B. (2016). *Biomimetics: Bioinspired Hierarchical-Structured Surfaces for Green Science and Technology*. Springer.

Bixler, G. D. and B. Bhushan (2013). Fluid drag reduction with shark-skin riblet inspired microstructured surfaces. *Advanced Functional Materials* 23 (36), 4507-4528.

Boomsma, A. and F. Sotiropoulos (2016). Direct numerical simulation of sharkskin denticles in turbulent channel flow. *Physics of Fluids* 28(3), 035106.

Caram, J. M. and A. Ahmed (1991). Effect of riblets on turbulence in the wake of an airfoil. *AIAA Journal* 29(11), 1769-1770.

Catalano, P., D. de Rosa, B. Mele, R. Tognaccini and F. Moens (2020). Performance improvements of a regional aircraft by riblets and natural laminar flow. *Journal of Aircraft* 57(1) 29-40.

Chen, H., F. Rao, X. Shang, D. Zhang and I. Hagiwara (2013). Biomimetic drag reduction study on herringbone riblets of bird feather. *Journal of Bionic Engineering* 10(3) 341-349.

Chen, H., F. Rao, X. Shang, D. Zhang and I. Hagiwara (2014). Flow over bio-inspired 3D herringbone wall riblets. *Experiments in Fluids* 55(3) 1698.

Chu, D. C. and G. E. Karniadakis (1993). A direct numerical simulation of laminar and turbulent flow over riblet-mounted surfaces. *Journal of Fluid Mechanics* 250, 1-42.

Dean, B. and B. Bhushan (2010). Shark-skin surfaces for fluid-drag reduction in turbulent flow: a review. *Philosophical Transactions of the Royal Society A: Mathematical, Physical and Engineering Sciences* 368(1929), 4775-4806.

Duan, L. and M. M. Choudhari (2014). Direct numerical simulations of high-speed turbulent boundary layers over riblets. In *52nd Aerospace Sciences Meeting,* 0934.

Fu, Y. F., C. Q. Yuan and X. Q. Bai (2017). Marine drag reduction of shark skin inspired riblet surfaces. *Biosurface and Biotribology* 3(1), 11-24.

Husen, N. M., J. W. Naughton and G. A. Dale (2020). Viscous drag on smooth and riblet surfaces. In *AIAA Scitech 2020 Forum*, 0309.

Ibrahim, M. D., S. N. A. Amran, Y. S. Yunos, M. R. A. Rahman, M. Z. Mohtar, L. K. Wong and A. Zulkharnain (2018). The study of drag reduction on ships inspired by simplified shark skin imitation. *Applied Bionics and Biomechanics.*

Jimenez, J. (1994). On the structure and control of near wall turbulence. *Physics of Fluids* 6(2), 944-953.

Koeltzsch, K., A. Dinkelacker and R. Grundmann (2002). Flow over convergent and divergent wall riblets. *Experiments in Fluids* 33(2), 346-350.

Koepplin, V., F. Herbst and J. R. Seume (2017). Correlation-based riblet model for turbomachinery applications. *Journal of Turbomachinery* 139(7), 071006.

Leitl, P. A., E. Göttlich, A. Flanschger, A. Peters, C. Feichtinger, A. Marn and B. Reschenhorfer (2020a). Numerical investigation of optimal riblet size for turbine center frame strut flow and the impact on the performance. In *AIAA Scitech 2020 Forum,* 0307.

Leitl, P. A., V. Stenzel, A. Flanschger, H. Kordy, C. Feichtinger, Y. Kowalik, S. Schreck and D. Stübing (2020b). Riblet Surfaces for Improvement of Efficiency of Wind Turbines. In *AIAA Scitech 2020 Forum,* 0308.

Li, W. (2020). Turbulence statistics of flow over a drag-reducing and a drag-increasing riblet-mounted surface. *Aerospace Science and Technology* 104, 106003.

Liu, Q., S. Zhong and L. Li (2017). Reduction of pressure losses in a linear cascade using herringbone riblets. In *ASME Turbo Expo: Power for Land, Sea, and Air.* 50787, V02AT39A025.

Martin, S. and B. Bhushan (2016a). Fluid flow analysis of continuous and segmented riblet structures. *Rsc Advances* 6(13), 10962-10978.

Martin, S. and B. Bhushan (2016b). Modeling and optimization of shark-inspired riblet geometries for low drag applications. *Journal of colloid and interface science* 474, 206-215.

Mele, B. and R. Tognaccini (2012). Numerical simulation of riblets on airfoils and wings. In *50th AIAA Aerospace Sciences Meeting Including the New Horizons Forum and*

Aerospace Exposition, 861.

Mele, B., L. Russo and R. Tognaccini (2020b). Drag bookkeeping on an aircraft with riblets and NLF control. *Aerospace Science and Technology* 98, 105714.

Mele, B., R. Tognaccini, P. Catalano and D. de Rosa (2020a). Analysis of riblets performance in pressure gradient flow by large eddy simulation. In *AIAA Scitech 2020 Forum*, 0031.

Park, J. and H. Choi (2017). Direct numerical simulation of flow over riblets with the yaw angle. In *APS Division of Fluid Dynamics Meeting Abstracts*, A16-009.

Sundaram, S., P. R. Viswanath and N. Subaschandar (1999). Viscous drag reduction using riblets on a swept wing. *AIAA Journal* 37(7), 851-856.

Sundaram, S., P. R. Viswanath and S. Rudrakumar (1996). Viscous drag reduction using riblets on NACA 0012 airfoil to moderate incidence. *AIAA Journal* 34(4), 676-682.

Walsh, M. J. (1983). Riblets as a viscous drag reduction technique. *AIAA Journal* 21(4), 485-486.

Wikipedia, The Free Encyclopedia 2020. Available online: http://en.wikipedia.org (accessed on August 2020).

Xu, F., S. Zhong and S. Zhang (2018). Vortical structures and development of laminar flow over convergent-divergent riblets. *Physics of Fluids* 30(5), 051901.

Yu, H. Y., H. C. Zhang, Y. Y. Guo, H. P. Tan, Y. Li and G. N. Xie (2016). Thermodynamic analysis of shark skin texture surfaces for microchannel flow. *Continuum Mechanics and Thermodynamics* 28(5), 1361-1371.

Zhang, Z., M. Zhang, C. Cai and K. Kang (2020). A general model for riblets simulation in turbulent flows. *International Journal of Computational Fluid Dynamics* 35(5), 333-345.

Zhou, H., X. Li and C. Yu (2020). Study on turbulence drag reduction of riblet plate in hypersonic turbulent flows. *International Journal of Modern Physics C* 31(3), 2050046.

Zhou, J., P. Ou and W. Wei (2018). Modeling of Turbulence Drag Reduction with Riblets. In *Asia-Pacific International Symposium on Aerospace Technology*, 614-629.